

COMPACT RECONSTRUCTION SCHEMES WITH WEIGHTED ENO LIMITING FOR HYPERBOLIC CONSERVATION LAWS*

DEBOJYOTI GHOSH[†] AND JAMES D. BAEDER[‡]

Abstract. The simulation of turbulent compressible flows requires an algorithm with high accuracy and spectral resolution to capture different length scales, as well as nonoscillatory behavior across discontinuities like shock waves. Compact schemes have the desired resolution properties and thus, coupled with a nonoscillatory limiter, are ideal candidates for the numerical solution of such flows. A class of compact-reconstruction weighted essentially non-oscillatory CRWENO schemes is presented in this paper where lower order compact stencils are identified at each interface and combined using the WENO weights. This yields a higher order compact scheme for smooth solutions with superior resolution and lower truncation errors, compared to the WENO schemes. Across discontinuities, the scheme reduces to a lower order nonoscillatory compact scheme by excluding stencils containing the discontinuity. The schemes are analyzed for scalar conservation laws in terms of accuracy, convergence, and computational expense, and extended to the Euler equations of fluid dynamics. The scalar reconstruction is applied to the conserved and characteristic variables. Numerical test cases are presented that show the benefits of these schemes over the traditional WENO schemes.

Key words. compact schemes, hyperbolic equations, implicit reconstruction, WENO limiting, Euler equations

AMS subject classifications. 35L04, 65M04, 76N04

DOI. 10.1137/110857659

1. Introduction. The solution of hyperbolic partial differential equations (PDEs) admits discontinuities, and thus numerical schemes require some form of limiting to be high order accurate for smooth solutions and nonoscillatory for discontinuous solutions [1, 2]. The essentially non-oscillatory (ENO) schemes were presented [3, 4, 5, 6] where the smoothest stencil is chosen amongst candidate stencils of the desired order for reconstruction at an interface. The ENO schemes were extended to the weighted essentially non-oscillatory (WENO) schemes [7, 8, 6] with no additional computational expense. A weighted combination of the candidate stencils is used to achieve a higher order of accuracy for smooth solutions, with the weights being a function of the smoothness of the corresponding stencils. Very high order WENO schemes have been constructed [9]. While arbitrarily high order accurate WENO schemes can be constructed, they suffer from poor spectral resolution and increasingly wide stencils.

Compact schemes were introduced [10] which achieve high orders of accuracy with smaller stencils by using implicit interpolations for the derivative of the function. The schemes were shown to have better bandwidth resolution and lower truncation errors for the same order of convergence. These schemes have been applied to the simulation of incompressible [11, 12] and compressible [13, 14] flows as well as to computational aeroacoustics [14, 15] and electromagnetics [16]. The improved resolution of compact schemes has resulted in their application to direct numerical simulation and large-

*Submitted to the journal's Methods and Algorithms for Scientific Computing section December 2, 2011; accepted for publication (in revised form) April 24, 2012; published electronically June 19, 2012.

<http://www.siam.org/journals/sisc/34-3/85765.html>

[†]Applied Mathematics & Statistics, and Scientific Computation, University of Maryland, College Park, MD 20740 (ghosh@umd.edu).

[‡]Aerospace Engineering, University of Maryland, College Park, MD 20740 (baeder@umd.edu).

eddy simulation of turbulent flows [17, 18, 19]. The compact schemes, originally formulated for finite differences on a uniform grid, have been extended to the finite volume formulation [20, 21] and nonuniform grids [22, 23, 24]. Linear compact schemes yield oscillatory solutions for flows with discontinuities, such as shock waves and contact discontinuities, and thus a limiter is needed to ensure nonoscillatory behavior. A nonlinearly stable compact scheme with a total variation bounded (TVB) limiter was introduced in [25] for shock calculations and further improved in [26].

There are several studies in the literature seeking to construct an algorithm with the nonoscillatory behavior of the ENO/WENO schemes as well as the improved spectral resolution of the compact schemes. Such algorithms would be ideal for the simulation of compressible turbulent flows, where small length scales as well as discontinuities need to be resolved accurately. A hybrid compact-ENO was presented [27] where the compact scheme is coupled with the ENO scheme. The smoothness of the solution is used to switch between the two schemes, and the resulting algorithm is shown to have an improved resolution in smooth regions of the solution, while maintaining nonoscillatory behavior across discontinuities. The algorithm was used for the direct numerical simulation of turbulent flow over a compression ramp [28]. A similar algorithm [29], coupling the compact schemes with WENO schemes, was presented and applied to shock-turbulence interactions. A conservative compact scheme was used for better coupling with the conservative WENO scheme and to ensure a globally conservative algorithm. The hybrid compact-WENO scheme was further improved [30] by introducing a smooth transition between the WENO and the compact scheme. Thus, the reconstructed flux is a weighted combination of the WENO and compact schemes where the weight depends on the smoothness of the solution. The hybrid scheme was also extended to the characteristic space to yield physically more robust solutions. While the hybrid schemes constructed show improved resolution while being nonoscillatory, they require indicators to detect discontinuities. They also suffer from the drawback that they switch to a noncompact scheme at and near discontinuities, thus resulting in a loss of resolution.

As an alternative to the hybrid schemes, a nonlinear compact scheme was presented [31] where adaptive stenciling (similar to the ENO algorithm) is used with candidate compact interpolations. Third and fourth order schemes were constructed. The scheme was extended in [32], where the WENO algorithm is used to compute the interface fluxes and a compact interpolation is used to compute high order finite difference approximations of the derivative at the cell center from the interface fluxes. While the earlier scheme required three tridiagonal inversions, corresponding to each of the three candidate ENO stencils (for a third order scheme), the improved scheme with the WENO reconstruction required just one such inversion. The scheme was further improved [33] by directly interpolating the fluxes instead of the conserved variables. A similar algorithm was described in [34], where a hybrid ENO-Padé scheme was constructed. A compact scheme is used to compute the derivatives at the cell centers from the interface values while the ENO scheme is used to reconstruct the interface values. These schemes show marginal improvement in their resolution characteristics because of the noncompact reconstruction at the interfaces. We would like to note here that the phrase “compact central WENO scheme” has been used to describe a central WENO algorithm with a 3-point stencil in [35]. However, the substencils in the WENO algorithm are not compact (in the sense that there is no coupling of the reconstruction or a derivative to increase the order of accuracy); they are noncompact second and third order stencils, with the final scheme being third order for smooth flows. Thus, their scheme is not truly compact (their order of accuracy is the same as the stencil

width) and lacks the spectral resolution properties of a compact (coupled) scheme.

A weighted compact scheme was constructed [36] where the final compact scheme was a weighted combination of compact substencils. In their implementation, the candidate stencils were two biased third order compact stencils and a central fourth order compact stencil. The optimal interpolation, for smooth solutions, was a sixth order central compact interpolation. While their work was a novel attempt at a nonoscillatory scheme, there were a few drawbacks. The underlying scheme, being central (and without additional dissipation), lacked the upwinding necessary to yield robust solutions to the Euler equations. The smoothness indicators that they use are the same as those of Jiang and Shu [8] and are designed for third order noncompact stencils. Their application to a fourth order central stencil may not have been correct. The extension of the scalar interpolation techniques to vector quantities is unclear in their study, and it is not discussed if their schemes were implemented in the characteristic space. It is well known that a characteristic reconstruction is necessary to yield nonoscillatory solutions for inviscid flow problems. These drawbacks resulted in limited applicability of their algorithm to the Euler system.

In the present paper, a class of compact-reconstruction WENO (CRWENO) schemes is constructed and extended to a system of equations. Our motivation is to implement a scheme that shows superior resolution for solutions with discontinuities as well as high-frequency signals. We employ the idea that is described in [36]; however, there are differences that result in a more robust scheme. At each interface, lower order compact stencils are identified as candidate stencils that can be combined with optimal weights to yield a higher order compact interpolation. In our implementation, the lower order candidate stencils, as well as the higher order optimal stencil, are biased compact interpolations, and thus our scheme is upwind. The higher order compact interpolation is shown to have superior spectral properties as compared to a noncompact interpolation of the same order (or even higher) and comparable resolution to compact schemes presented in the literature [10, 32]. The WENO limiting is applied to these weights, and it is observed that the smoothness indicators of Jiang and Shu work well with our compact substencils, thus yielding nonoscillatory solutions. The final interpolation scheme results in a tridiagonal system of equations. However, it should be noted that, unlike compact schemes previously presented in the literature (except that in [36]), the coefficients in our tridiagonal system are a function of the stencil weights, which are solution-dependent. Thus, a prefactoring of the system of equations is not possible and a tridiagonal inversion is required at each time step. The scalar interpolation scheme thus described is extended to the Euler equations of fluid dynamics, which are a system of hyperbolic conservation laws. The compact interpolation, with the WENO limiting, is carried out on either the conserved or the characteristic variables. While the application of the compact schemes to the conserved variables is a trivial extension of the scalar algorithm, the application on the characteristic variables requires the solution of a block tridiagonal system of equations at each iteration.

The paper is outlined as follows. Section 2 describes the numerical method and discretization of a scalar hyperbolic PDE as well as the time marching procedure used in the present study. Section 3 describes the conventional WENO schemes and introduces the CRWENO schemes. The fifth order WENO and CRWENO schemes are described in detail since they are used for numerical studies. Boundary treatment and the computational expense of the new schemes are discussed. Section 4 applies these schemes to two scalar conservation laws: the linear advection equation and the inviscid Burgers equation. Smooth solutions are used to study the error and

convergence properties of the schemes, while discontinuous solutions with different waveforms are used to assess the behavior of the schemes on different discontinuities. The computational expense of the new schemes is studied and compared to that of the WENO scheme. The extension of these schemes to the Euler equations of fluid dynamics is discussed in section 5. Section 6 applies the compact schemes to different one- and two-dimensional flow cases. Conclusions are presented in section 7.

2. Numerical method and discretization. A generic scalar conservation law in one space dimension can be expressed as

$$(2.1) \quad u_t + f_x = 0,$$

where $u(x, t)$ is the conserved quantity and $f(x, t) = f(u(x, t))$ is the flux function. The subscripts denote partial derivatives and t and x are time and distance, respectively. Equation (2.1) is discretized on a uniformly spaced grid where j is the grid index, x_j is the cell center of the j th cell, and $x_{j+1/2}$ is the interface between cells j and $j + 1$. A conservative finite difference discretization of (2.1) results in an ordinary differential equation (ODE), expressed as

$$(2.2) \quad \frac{du_j}{dt} + \frac{1}{\Delta x} [h(x_{j+1/2}, t) - h(x_{j-1/2}, t)] = 0,$$

where $u_j = u(x_j, t)$ is the cell-centered value of $u(x, t)$ in cell j . The numerical flux function $h(x)$ is required to satisfy exactly [5]

$$(2.3) \quad \left. \frac{\partial f}{\partial x} \right|_{x=x_j} = \frac{1}{\Delta x} [h(x_{j+1/2}, t) - h(x_{j-1/2}, t)]$$

and can thus be defined implicitly as

$$(2.4) \quad f(x) = \frac{1}{\Delta x} \int_{x-\Delta x/2}^{x+\Delta x/2} h(\xi) d\xi.$$

The approximation of the numerical flux at the interfaces $h(x_{j+1/2})$ from the discrete values of flux $f(x_j)$ at cell centers is the reconstruction step outlined in the next section. Equation (2.2) can be solved using any ODE solver by discretizing in time where n is the time index, dt is the time-step size, $t^n = ndt$ is the n th time level, and $u^n = u(x, t^n)$ is the solution at t^n . The Euler explicit scheme results in first order accuracy. In the present study, the third order total variation diminishing Runge–Kutta (TVD-RK3) scheme [4] is used with higher order reconstruction. Given the solution at t^n , the solution at t^{n+1} can be obtained as

$$(2.5) \quad \begin{aligned} v^{(0)} &= u^n, \\ v^{(1)} &= v^{(0)} + \sigma L(v^{(0)}), \\ v^{(2)} &= \frac{3}{4}v^{(0)} + \frac{1}{4}(v^{(1)} + \sigma L(v^{(1)})), \\ v^{(3)} &= \frac{1}{3}v^{(0)} + \frac{2}{3}(v^{(2)} + \sigma L(v^{(2)})), \\ u^{n+1} &= v^{(3)}, \end{aligned}$$

where σ is the CFL number. The residual function $L(u)$ is

$$(2.6) \quad L(u) = -[h(x_{j+1/2}, t) - h(x_{j-1/2}, t)].$$

Thus, given initial conditions $u(x, 0) = u_0(x)$, (2.1) can be numerically solved to yield the solution $u(x, t)$ at any given time.

3. Reconstruction. The solution of a hyperbolic PDE or a system of equations is composed of waves. A scalar solution comprises a right or left running wave. The reconstruction of the numerical flux at the interfaces models this wave phenomenon through upwinding. At each interface, the flux can be approximated using a left or right biased interpolation. The appropriate interpolation is chosen based on the sign of the wave speed, which in the case of a scalar PDE is given by $f'(u)$.

$$(3.1) \quad \begin{aligned} h_{j+1/2} &= h_{j+1/2}^L \text{ if } f'(u)|_{x=x_{j+1/2}} > 0, \\ &= h_{j+1/2}^R \text{ if } f'(u)|_{x=x_{j+1/2}} < 0, \end{aligned}$$

where the superscripts L and R denote left and right biased interpolations respectively. The approximation of the left biased numerical flux $h_{j+1/2}^L$ is described in this section. The approximation of the right biased flux $h_{j+1/2}^R$ follows a similar process. The superscripts are omitted in the subsequent description.

The reconstruction process seeks to approximate the numerical flux to the desired order; i.e., we find an approximate flux function $\hat{f}(x) \approx h(x)$ such that

$$(3.2) \quad \begin{aligned} \left. \frac{\partial f}{\partial x} \right|_{x=x_j} &= \frac{h_{j+1/2} - h_{j-1/2}}{\Delta x} \\ &= \frac{\hat{f}_{j+1/2} - \hat{f}_{j-1/2}}{\Delta x} + O(\Delta x^r), \end{aligned}$$

where r is the desired order of the scheme. As an example of noncompact interpolations, for $r = 5$, we have

$$(3.3) \quad \begin{aligned} \hat{f}_{j+1/2} &= \frac{1}{30}f_{j-2} - \frac{13}{60}f_{j-1} + \frac{47}{60}f_j + \frac{27}{60}f_{j+1} - \frac{1}{20}f_{j+2} \\ &= h_{j+1/2} - \frac{1}{60} \left. \frac{\partial^5 f}{\partial x^5} \right|_{x=x_j} \Delta x^5 + O(\Delta x^6). \end{aligned}$$

A fifth order compact interpolation is given by

$$(3.4) \quad \frac{3}{10}\hat{f}_{j-1/2} + \frac{6}{10}\hat{f}_{j+1/2} + \frac{1}{10}\hat{f}_{j+3/2} = \frac{1}{30}f_{j-1} + \frac{19}{30}f_j + \frac{10}{30}f_{j+1},$$

which gives an error of

$$(3.5) \quad \hat{f}_{j+1/2} = h_{j+1/2} - \frac{1}{600} \left. \frac{\partial^5 f}{\partial x^5} \right|_{x=x_j} \Delta x^5 + O(\Delta x^6).$$

Thus, the magnitude of the leading error term in the compact interpolation is an order of magnitude less than the corresponding noncompact interpolation of the same order. Figures 3.1(a) and 3.1(b) show the dispersion and dissipation characteristics of the noncompact and compact fifth order schemes. The compact scheme is much better at resolving higher frequencies. It can be seen that the fifth order compact scheme has a better spectral fidelity than the ninth order noncompact scheme. Although the compact scheme is more dissipative at higher frequencies, the phase error is large there for all schemes and the higher dissipation helps in filtering out high-frequency errors. At frequencies where the phase error is low, the compact fifth order scheme has less dissipation than the noncompact fifth order scheme and is comparable to the ninth order noncompact scheme.

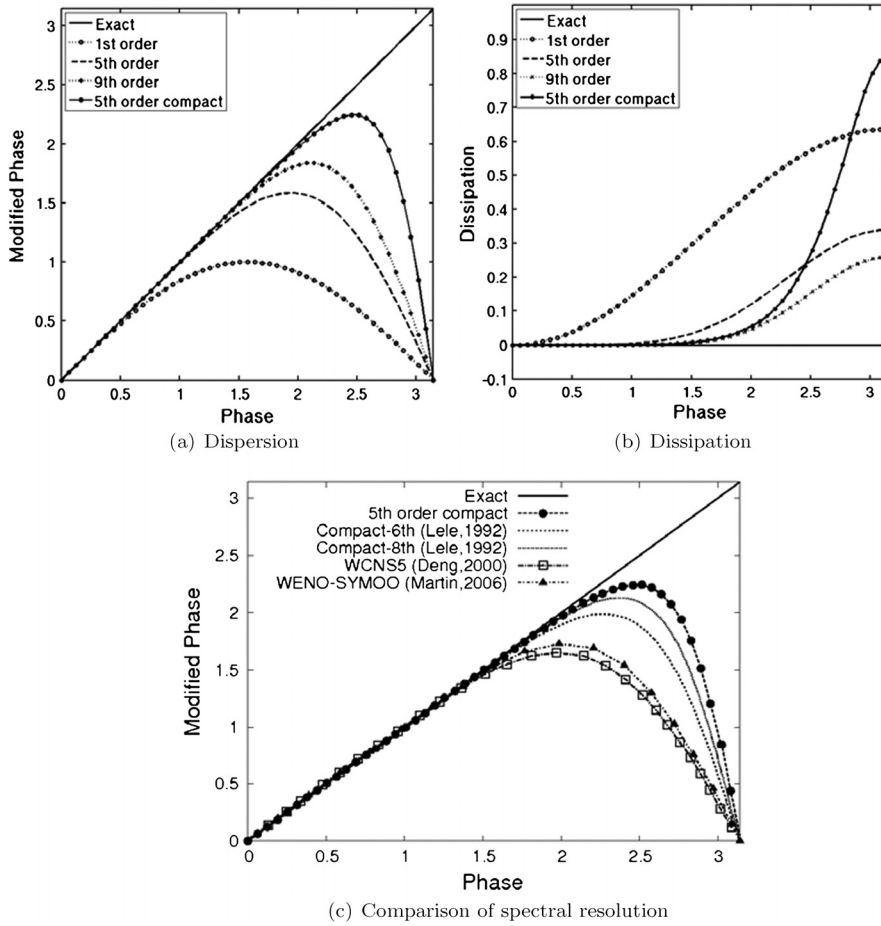


FIG. 3.1. Spectral characteristics of the first order, noncompact fifth order, noncompact ninth order and compact fifth order schemes, and comparison of the present scheme with previously published compact and optimized schemes

The spectral fidelity of the schemes can be quantified by the “bandwidth-resolving efficiency” [10], which is the phase (as a fraction of π) at which the error in the modified phase exceeds 0.01. The bandwidth-resolving efficiency is 0.35 for the fifth order noncompact interpolation (3.3) with a 5-point stencil, 0.42 for a seventh order noncompact interpolation with a 7-point stencil, and 0.48 for a ninth order noncompact interpolation with a 9-point stencil. The fifth order compact scheme (3.4) with a 3-point stencil achieves an efficiency of 0.6, which shows a significant improvement over these noncompact schemes. This compares well with the efficiencies of the central compact schemes introduced by Lele [10] (0.58 for an eighth order tridiagonal scheme and 0.61 for an eighth order pentadiagonal scheme). Bandwidth-optimized WENO schemes have been presented for direct numerical simulation of turbulent flows [37] where a symmetric stencil is used for interpolation with biased coefficients for upwinding. The coefficients are such that the dissipation and dispersion errors are minimized and the bandwidth is maximized. The resulting improved bandwidth-resolving efficiencies of these noncompact interpolation schemes are 0.49 for a scheme with a 6-point stencil and 0.56 for a scheme with an 8-point stencil. These are still lower than that of the fifth order compact scheme.

Figure 3.1(c) shows a comparison of the spectral resolution of the fifth order compact scheme, (3.4), with compact and resolution-optimized schemes in the literature. The schemes “Compact-6th” and “Compact-8th” refer to the sixth and eighth order tridiagonal schemes of Lele [10], respectively. The fifth order weighted compact nonlinear scheme [32], “WCNS5,” uses a cell-centered compact scheme (sixth order) for computing the derivatives. However, the interface values are computed using the noncompact WENO scheme, and thus the resolution of the scheme is only marginally better than a regular fifth order scheme. The scheme “WENO-SYMOO” refers to the optimized WENO scheme [37] ($r = 4$, which would have yielded a seventh order scheme without the optimization) for improved bandwidth resolution, proposed for the direct numerical simulation of turbulence. The fifth order compact scheme, which is the basis of our compact-reconstruction WENO schemes, compares favorably with these schemes.

The fifth order compact interpolation, (3.4), uses a biased 3-point stencil ($j - 1, j, j + 1$) to compute the interface flux at $j + 1/2$. A sixth order compact interpolation can be constructed with the stencil ($j - 1, j, j + 1, j + 2$), which is symmetric. Such an interpolation would be central and thus would not have the upwinding required to give stable solutions. However, with biased coefficients, a fifth order compact interpolation can be constructed with the symmetric stencil, given by

$$(3.6) \quad \frac{5}{20}\hat{f}_{j-1/2} + \frac{12}{20}\hat{f}_{j+1/2} + \frac{3}{20}\hat{f}_{j+3/2} = \frac{1}{120}(3f_{j-1} + 67f_j + 49f_{j+1} + f_{j+2}),$$

resulting in an even lower absolute error of

$$(3.7) \quad \hat{f}_{j+1/2} = h_{j+1/2} - \frac{1}{1200} \left. \frac{\partial^5 f}{\partial x^5} \right|_{x=x_j} \Delta x^5 + O(\Delta x^6).$$

The left biased low-dissipation compact interpolation uses a wider stencil by including data at the $(j + 2)$ th grid cell. However, for systems of equations, as discussed in subsequent sections, the final flux is a combination of the left and right biased fluxes. The computation of the right biased flux with a fifth order compact interpolation would use the stencil ($j, j + 1, j + 2$), and the overall stencil for the calculation of the flux at the $(j + 1/2)$ th interface would be ($j - 1, j, j + 1, j + 2$). Thus, an algorithm based on the low-dissipation compact interpolation does not use data from a wider stencil, compared to the compact interpolation.

Hyperbolic conservation laws admit discontinuous solutions, and these interpolation schemes suffer from oscillations across discontinuities. The WENO schemes use adaptive stenciling to achieve the high order of accuracy at smooth regions of the solution while switching to lower order interpolation to avoid oscillations near discontinuities.

3.1. WENO schemes. The WENO schemes [7, 8] are based on the idea of combining lower order candidate stencils at an interface to get a higher order interpolation in smooth regions and a nonoscillatory interpolation near discontinuities. The general form of the interface flux reconstructed by the WENO scheme is

$$(3.8) \quad \hat{f}_{j+1/2} = \sum_{k=1}^r \omega_k \hat{f}_{j+1/2}^k,$$

where r is the number of candidate stencils (of r th order), $\hat{f}_{j+1/2}^k$ is the interpolated flux at $x_{j+1/2}$ using the k th candidate stencil, and ω_k is the weight of k th stencil

in the convex combination. There exist optimal weights c_k , $k = 1, \dots, r$, such that if $\omega_k = c_k \forall k$, the resulting interpolation is $(2r - 1)$ th order accurate. The WENO limiting process causes the stencil weights to attain their optimal values where the solution is smooth. Across or near a discontinuity, the weight of the stencil containing the discontinuity approaches zero to yield a nonoscillatory interpolated flux. This is achieved by scaling the optimal weights by smoothness indicators of the respective stencils [8], i.e.,

$$(3.9) \quad \alpha_k = \frac{c_k}{(\beta_k + \epsilon)^m},$$

where β_k is the smoothness indicator of the k th stencil, ϵ is a small number to prevent division by zero, and m is chosen such that the weights for nonsmooth stencils approach zero quickly (in the present study, $m = 2$ is used for all cases). To ensure convexity, the weights α_k are normalized as

$$(3.10) \quad \omega_k = \frac{\alpha_k}{\sum_k \alpha_k}.$$

The resulting interpolation is thus $(2r - 1)$ th order accurate in smooth regions of the solution and nonoscillatory near discontinuities.

The weights, (3.9), have been shown to be excessively dissipative and a loss of accuracy has been observed for smooth solutions with vanishing derivatives. Several attempts have been presented in the literature that improve the behavior of the WENO schemes for such cases. A mapping of the weights has been proposed [38] that causes the WENO weights to converge faster to their optimal values, defined by the function

$$(3.11) \quad g_k(\omega) = \frac{\omega(c_k + c_k^2 - 3c_k\omega + \omega^2)}{c_k^2 + \omega(1 - 2c_k)}.$$

The new weights are given by

$$(3.12) \quad \alpha_k^M = g_k(\omega_k),$$

which are then normalized for convexity to give the mapped WENO weights. The primary drawback of the mapping is the additional computational cost of the mapping function. Alternative formulations for the weights have been suggested in the literature [39, 40] which have the same benefits as the mapping function without the additional expense. The weights are defined as

$$(3.13) \quad \alpha_k = c_k \left(1 + \frac{\tau}{\epsilon + \beta_k} \right).$$

The factor τ is defined as the absolute difference between the leftmost and rightmost smoothness indicators by [39], while it is defined as the square of the divided difference of the appropriate order by [40]. A complete discussion of the relative merits and demerits of these approaches is outside the scope of this paper, and the results presented here use the mapping of the weights. However, our CRWENO schemes can be used with the weights defined by (3.13) as well with only minor differences in the solutions for long-term convections, and the analyses and conclusions are identical to those that we present in this paper.

The fifth order WENO scheme of Jiang and Shu [8] ($r = 3$) is constructed by combining three third order candidate interpolations, given by

$$(3.14) \quad \hat{f}_{j+1/2}^1 = \frac{1}{3}f_{j-2} - \frac{7}{6}f_{j-1} + \frac{11}{6}f_j,$$

$$(3.15) \quad \hat{f}_{j+1/2}^2 = -\frac{1}{6}f_{j-1} + \frac{5}{6}f_j + \frac{1}{3}f_{j+1},$$

$$(3.16) \quad \hat{f}_{j+1/2}^3 = \frac{1}{3}f_j + \frac{5}{6}f_{j+1} - \frac{1}{6}f_{j+2}.$$

The optimal weights are $c_1 = 1/10$, $c_2 = 6/10$, $c_3 = 3/10$, which yield the fifth order interpolation, (3.3). The weights can thus be computed using (3.9) and (3.10), and the final form of the WENO5 scheme can be expressed as

$$(3.17) \quad \begin{aligned} \hat{f}_{j+1/2} &= \frac{\omega_1}{3}f_{j-2} - \frac{1}{6}(7\omega_1 + \omega_2)f_{j-1} + \frac{1}{6}(11\omega_1 + 5\omega_2 + 2\omega_3)f_j \\ &+ \frac{1}{6}(2\omega_2 + 5\omega_3)f_{j+1} - \frac{\omega_3}{6}f_{j+2}. \end{aligned}$$

The smoothness indicators are given by

$$(3.18) \quad \beta_1 = \frac{13}{12}(f_{j-2} - 2f_{j-1} + f_j)^2 + \frac{1}{4}(f_{j-2} - 4f_{j-1} + 3f_j)^2,$$

$$(3.19) \quad \beta_2 = \frac{13}{12}(f_{j-1} - 2f_j + f_{j+1})^2 + \frac{1}{4}(f_{j-1} - f_{j+1})^2,$$

$$(3.20) \quad \beta_3 = \frac{13}{12}(f_j - 2f_{j+1} + f_{j+2})^2 + \frac{1}{4}(3f_j - 4f_{j+1} + f_{j+2})^2.$$

Higher order WENO schemes with $r = 4, 5, 6$ have been constructed [9]. While the schemes have very high orders of accuracy, the primary drawback is the minimal increase in spectral resolution along with interpolation over wide stencils.

3.2. CRWENO schemes. While higher order WENO schemes based on noncompact interpolation have been constructed, their primary drawback is the increasingly wide stencil as we increase the order of accuracy. A class of WENO schemes is presented which use implicit interpolation with compact stencils as their basis. The CRWENO schemes follow the same procedure as WENO schemes, (3.8)–(3.10). The candidate interpolations are, however, implicit, resulting in smaller stencils. In the present section, the construction of the fifth order CRWENO schemes is described.

The fifth order CRWENO scheme (CRWENO5) is constructed using three third order compact interpolations as candidates. They are

$$(3.21) \quad \frac{2}{3}\hat{f}_{j-1/2}^1 + \frac{1}{3}\hat{f}_{j+1/2}^1 = \frac{1}{6}(f_{j-1} + 5f_j),$$

$$(3.22) \quad \frac{1}{3}\hat{f}_{j-1/2}^2 + \frac{2}{3}\hat{f}_{j+1/2}^2 = \frac{1}{6}(5f_j + f_{j+1}),$$

$$(3.23) \quad \frac{2}{3}\hat{f}_{j+1/2}^3 + \frac{1}{3}\hat{f}_{j+3/2}^3 = \frac{1}{6}(f_j + 5f_{j+1}).$$

The optimal weights are $c_1 = 1/5$, $c_2 = 1/2$, $c_3 = 3/10$, which result in the fifth order compact interpolation (3.4). The smoothness indicators, (3.18)–(3.20), are used to compute the weights of each stencil, resulting in an implicit system given by

$$(3.24) \quad \begin{aligned} &\left(\frac{2}{3}\omega_1 + \frac{1}{3}\omega_2\right)\hat{f}_{j-1/2} + \left[\frac{1}{3}\omega_1 + \frac{2}{3}(\omega_2 + \omega_3)\right]\hat{f}_{j+1/2} + \frac{1}{3}\omega_3\hat{f}_{j+3/2} \\ &= \frac{\omega_1}{6}f_{j-1} + \frac{5(\omega_1 + \omega_2) + \omega_3}{6}f_j + \frac{\omega_2 + 5\omega_3}{6}f_{j+1}. \end{aligned}$$

The left-hand side is a tridiagonal system, and the convexity of the weights ensures that none of the main diagonal elements is zero.

A low-dissipation CRWENO scheme (CRWENO5-LD) is constructed based on the low-dissipation compact interpolation (3.6). The scheme is a combination of four candidate stencils, three of which are (3.21)–(3.23). The fourth stencil is

$$(3.25) \quad \frac{1}{3}\hat{f}_{j+1/2}^4 + \frac{2}{3}\hat{f}_{j+3/2}^4 = \frac{1}{6}(5f_{j+1} + f_{j+2}).$$

The optimal weights are $c_1 = 3/20, c_2 = 9/20, c_3 = 7/20, c_4 = 1/20$. While the same smoothness indicators are used for the first three stencils, the smoothness indicator for the fourth stencil is expressed as

$$(3.26) \quad \beta_4 = \frac{13}{12}(f_{j+1} - 2f_{j+2} + f_{j+3})^2 + \frac{1}{4}(-5f_{j+1} + 8f_{j+2} - 3f_{j+3})^2, \\ \beta_4 = \max(\beta_3, \beta_4).$$

The fourth smoothness indicator is taken as a maximum of itself and the third smoothness indicator to ensure that the weight for the fourth stencil is always less than or equal to the third stencil, thus preventing a completely downwind interpolation. The resulting scheme can be expressed as

$$(3.27) \quad \frac{2\omega_1 + \omega_2}{3}\hat{f}_{j-1/2} + \frac{\omega_1 + 2(\omega_2 + \omega_3) + \omega_4}{3}\hat{f}_{j+1/2} + \frac{\omega_3 + 2\omega_4}{3}\hat{f}_{j+3/2} \\ = \frac{\omega_1}{6}f_{j-1} + \frac{5(\omega_1 + \omega_2) + \omega_3}{6}f_j + \frac{\omega_2 + 5(\omega_3 + \omega_4)}{6}f_{j+1} + \frac{\omega_4}{6}f_{j+2}.$$

In smooth regions of the solution, where the weights attain their optimal values, the CRWENO5-LD scheme is theoretically expected to give half the absolute error of the CRWENO5 scheme.

The CRWENO schemes result in a globally coupled tridiagonal system of equations for the interface fluxes for a smooth solution, as is characteristic of compact schemes. However, coupling across discontinuities introduce nonphysical oscillations, and this is avoided in our schemes by the WENO weights, which essentially decouples the subdomains on either side of the discontinuity. Adjacent to a discontinuity, the corresponding weight approaches zero and the equation for the interface flux reduces to a biased bidiagonal equation. Thus, discontinuities in the solution partition the domain, and the fluxes are reconstructed in a coupled fashion within each smooth subdomain. At the discontinuity, the scheme employs a third order compact interpolation which has a better spectral resolution than a third order noncompact scheme. Hybrid compact-ENO/WENO schemes [27, 29, 30], on the other hand, use a noncompact interpolation across and near discontinuities, thus compromising on the resolution of the scheme at these critical points.

3.3. Boundary treatment. The CRWENO schemes described above apply to interior interfaces. Thus, they can be applied at all interfaces for problems with periodic/infinite boundary conditions. This results in a periodic tridiagonal system which can be solved with $O(N)$ complexity, where N is the number of grid points. Aperiodic problems require special treatment at the boundary interfaces where (3.24) and (3.27) do not apply. It should be noted that for a multidimensional domain, the compact scheme described here is implicit along each dimension, and the linear system of equations, with the appropriate boundary treatment, is solved separately

for each grid line, at interfaces along each dimension. In our implementation, the flux at the boundary interfaces, i.e., the first and last interfaces along each grid line, is reconstructed using the WENO5 procedure (3.17). The resulting tridiagonal system of equations can be represented as

$$(3.28) \quad \begin{bmatrix} 1 & 0 & 0 & \dots & \dots & \dots & 0 \\ a & b & c & 0 & \dots & \dots & 0 \\ \cdot & & \cdot & & & & \cdot \\ \cdot & & & \cdot & & & \cdot \\ \cdot & & & & \cdot & & \cdot \\ 0 & \dots & \dots & 0 & a & b & c \\ 0 & \dots & \dots & \dots & 0 & 0 & 1 \end{bmatrix} \begin{pmatrix} \hat{f}_{1/2} \\ \cdot \\ \cdot \\ \hat{f}_{j+1/2} \\ \cdot \\ \cdot \\ \hat{f}_{NJ+1/2} \end{pmatrix} = \begin{pmatrix} \hat{r}_{1/2}^{WENO5} \\ \cdot \\ \cdot \\ \hat{r}_{j+1/2}^{CRWENO5} \\ \cdot \\ \cdot \\ \hat{r}_{NJ+1/2}^{WENO5} \end{pmatrix},$$

where NJ is the total number of grid points, \hat{r}^{WENO5} is the right-hand side of (3.17), and $\hat{r}^{CRWENO5}$ is the right-hand side of (3.24) or (3.27). The coefficients a , b , and c represent the coefficients on the left-hand side of (3.24) or (3.27). Our numerical tests do not show any loss of accuracy or resolution due to this boundary treatment. The data required by the WENO5 scheme at the boundaries are provided by using ghost points.

3.4. Computational expense. The CRWENO5 and CRWENO5-LD schemes result in a tridiagonal system of equations, represented by (3.28). The WENO weights, and thus the coefficients in the matrix, are solution-dependent, and therefore the tridiagonal matrix inversion is needed at each iteration. A one-dimensional problem requires one matrix inversion, while for multidimensional problems, a tridiagonal inversion is required along each grid line, along each dimension. As an example, for a two-dimensional domain, discretized by an $NI \times NJ$ mesh, the compact schemes require $(NI + NJ)$ tridiagonal inversions. While the tridiagonal inversion is of $O(N)$ complexity, scaling linearly with the number of mesh points, this introduces a computational overhead.

However, the spectral properties of the compact schemes imply that coarser grids may be used to achieve the same resolution as a noncompact scheme of the same order of convergence. Taylor series analysis predicts an error that is a tenth of the noncompact scheme of the same order, as shown in previous sections. Thus, for fifth order convergence, the WENO5 scheme would require a grid that is $10^{1/5}$ or 1.6 times as fine to achieve the same accuracy as the CRWENO5 scheme, and a grid that is $20^{1/5}$ or 1.8 times as fine to achieve the same accuracy as the CRWENO5-LD scheme. These represent substantial savings in the computational expense and are amplified in multidimensions. The computational efficiency of the CRWENO schemes are studied in the following sections, and results comparing the errors and run-times of the WENO5, CRWENO5, and CRWENO5-LD schemes are presented.

4. Numerical results: Scalar equations. The compact schemes presented in the previous section are analyzed. Their behavior, in terms of accuracy and convergence properties, is studied on the linear advection equation and the inviscid Burgers equation. The schemes are tested on both smooth and nonsmooth data and compared with WENO schemes. The linear advection equation is the simplest example of a scalar hyperbolic PDE, while the inviscid Burgers equation is an example of a scalar nonlinear hyperbolic PDE. The convergence behavior of the schemes is studied on smooth problems for which the exact solution is known. The behavior of CRWENO schemes across discontinuities is compared with that of the WENO schemes.

The first order scheme is used with Euler explicit time marching, while the fifth order WENO and CRWENO schemes are used with TVD-RK3 time marching in all cases.

4.1. Linear advection equation. The linear advection equation is given by

$$(4.1) \quad u_t + u_x = 0.$$

The flux function in (2.1) for the advection equation is $f(u) = u$. Given an initial condition $u(x, 0) = u_0(x)$, the exact solution at any time is given by

$$(4.2) \quad u(x, t) = u_0(x - t).$$

The solution consists of a single wave running in the positive x -direction. Thus, during the reconstruction process, the left biased interpolations are used in (3.1).

The convergence properties of the schemes are tested using an example with smooth data. The domain is $-1 \leq x \leq 1$ and the initial condition is specified as

$$(4.3) \quad u_0(x) = \sin\left(\pi x - \frac{\sin(\pi x)}{\pi}\right).$$

Periodic boundary conditions are used and the solution is obtained after one cycle over the periodic domain. Tables 4.1 and 4.2 show the L_2 errors and convergence rates (r_c) for the WENO5, CRWENO5, and CRWENO5-LD schemes, along with the Explicit5 (3.3), Implicit5 (3.4) and the Implicit5-LD (3.6) schemes that they are based on. The grid was progressively refined from 20 points to 640 points for the error and convergence analysis. The initial CFL (for the grid of 20 points) is 0.1 and is reduced by a factor of $2/(2^{5/3})$ at each refinement (since the spatial interpolation is fifth order and time marching is third order, this ensures that time discretization errors converge at the same rate as the space discretization ones). A low CFL number is chosen to ensure that the errors due to time discretization are significantly lower than those due to space discretization. Figure 4.1(a) shows the L_2 norm of the errors for the different schemes as a function of the number of grid points. The smoothness indicators, and thus the errors and convergence behaviors, show some irregularities at very coarse grids for all the schemes. However, as the grids are refined, the WENO weights converge to their optimal values for this smooth problem. The errors and convergence behaviors are identical for each of the WENO scheme and its optimal counterpart. The errors for the CRWENO5 and Implicit5 schemes are almost an order of magnitude lower than those for the WENO5 and Explicit5 schemes at all grid levels. The errors from CRWENO5-LD and Implicit5-LD are almost half of those from CRWENO5 and Implicit5 for finer grids. These observations are consistent with the Taylor series

TABLE 4.1

L_2 errors and convergence rates for *Explicit5*, *Implicit5*, and *Implicit5-LD* with smooth initial data (linear advection).

N	Explicit5		Implicit5		Implicit5-LD	
	Error	r_c	Error	r_c	Error	r_c
20	2.729E-03	-	3.520E-04	-	1.981E-04	-
40	9.639E-05	4.82	1.052E-05	5.06	5.599E-06	5.15
80	3.077E-06	4.97	3.244E-07	5.02	1.704E-07	5.04
160	9.664E-08	4.99	1.011E-08	5.00	5.291E-09	5.01
320	3.024E-09	5.00	3.157E-10	5.00	1.653E-10	5.00
640	9.508E-11	4.99	1.075E-11	4.88	6.335E-12	4.71

TABLE 4.2

L_2 errors and convergence rates for WENO5, CRWENO5, and CRWENO5-LD with smooth initial data (linear advection).

N	WENO5		CRWENO5		CRWENO5-LD	
	Error	r_c	Error	r_c	Error	r_c
20	2.250E-03	-	6.508E-04	-	6.919E-04	-
40	9.414E-05	4.58	1.247E-05	5.71	9.644E-06	6.17
80	3.069E-06	4.94	3.390E-07	5.20	2.027E-07	5.57
160	9.663E-08	4.99	1.024E-08	5.05	5.569E-09	5.19
320	3.024E-09	5.00	3.171E-10	5.01	1.679E-10	5.05
640	9.509E-11	4.99	1.077E-11	4.88	6.357E-12	4.72

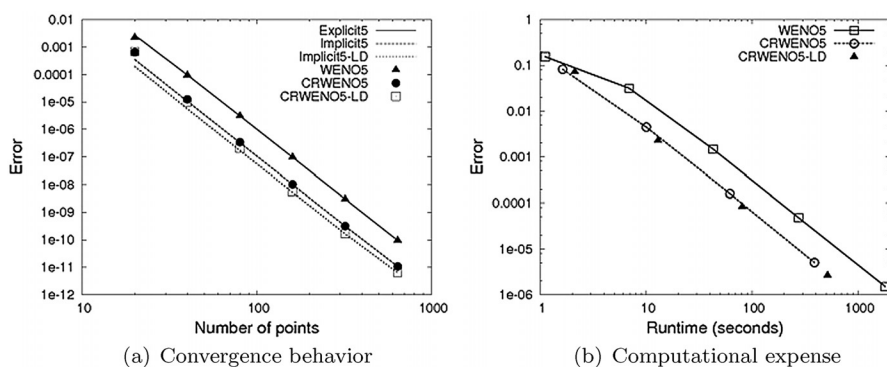


FIG. 4.1. L_2 error and numerical cost of different schemes for the linear advection equation.

analysis of these schemes. Thus, at the same grid resolution, the compact schemes show significantly lower absolute errors for the same order of convergence.

The compact schemes require the solution of a tridiagonal system of equations and are computationally more expensive than the WENO scheme. The weights, and thus the coefficients of the left-hand side of the system of equations, are solution-dependent and the linear system is required to be solved at each iteration. Table 4.3 shows the L_2 norm of the error and the computational run-time (T) for the WENO5, CRWENO5 and CRWENO5-LD schemes for different grid resolutions after 500 cycles over the periodic domain. The CFL for the initial grid of 20 points is 0.1 and is reduced as described previously, to maintain fifth order accuracy. The CRWENO5 and CRWENO5-LD schemes are computationally more expensive at the same grid

TABLE 4.3

L_2 errors and computational run-time (in seconds) for WENO5, CRWENO5, and CRWENO5-LD with smooth initial data (linear advection).

N	WENO5		CRWENO5		CRWENO5-LD	
	Error	T	Error	T	Error	T
20	1.549E-01	1.11	8.236E-02	1.62	7.201E-02	2.11
30	8.416E-02	2.45	-	-	-	-
40	3.155E-02	6.89	4.436E-03	10.02	2.277E-03	12.94
60	5.729E-03	15.20	-	-	-	-
80	1.480E-03	42.73	1.603E-04	61.66	8.343E-05	80.53
120	2.033E-04	95.28	-	-	-	-
160	4.824E-05	268.85	5.047E-06	388.24	2.635E-06	516.89
240	6.404E-06	602.76	-	-	-	-

resolution. However, the absolute errors are an order of magnitude lower than the WENO5 scheme. A comparison of the computational expense is made for solutions having the same order of absolute errors. The CRWENO5 scheme yields errors that are a tenth of the WENO5 scheme, thus it is expected that the WENO5 scheme will yield the same error on a grid that has 1.6 times more points. The table shows the errors and run-times for the WENO5 schemes on grids with 30, 60, 120, and 240 points for which the errors are of the same order of magnitude as the compact schemes on grids with 20, 40, 80, and 160 points, respectively. It is observed that the compact schemes require lower grid resolutions, and thus lower computational expense, to yield solutions with comparable errors. Figure 4.1(b) shows the L_2 norm of the error as a function of the run-time for the WENO5, CRWENO5, and CRWENO5-LD schemes. The previous observation is reiterated: while the compact schemes are more expensive at the same grid resolution, they are substantially less expensive for similar absolute errors in the solution.

The behavior of the schemes across discontinuities is analyzed for a case comprising a square wave, an exponential wave, a triangular wave, and a parabolic wave. The initial conditions are given by

$$\begin{aligned}
 u_0(x) &= \exp\left(-\log(2)\frac{(x+7)^2}{0.0009}\right) \text{ if } -0.8 \leq x \leq -0.6 \\
 &= 1 \text{ if } -0.4 \leq x \leq -0.2 \\
 &= 1 - |10(x-0.1)| \text{ if } 0 \leq x \leq 0.2 \\
 &= [1 - 100(x-0.5)^2]^{(1/2)} \text{ if } 0.4 \leq x \leq 0.6 \\
 &= 0 \text{ otherwise,}
 \end{aligned}
 \tag{4.4}$$

where the domain is $-1 \leq x \leq 1$. Periodic boundary conditions are applied and the solution is obtained after one cycle over the domain at a CFL of 0.5.

Figure 4.2(a) shows the solution on a grid with 160 points for the WENO5, CRWENO5, and CRWENO5-LD schemes at a CFL of 0.5, while Figures 4.2(b) and Figure 4.2(c) show the magnified solution for the exponential and square waves. The CRWENO5 and CRWENO5-LD schemes are seen to be nonoscillatory, thus validating that the smoothness indicators and the WENO weights work well with the compact stencils. Across the discontinuities, the compact schemes are less dissipative than the WENO5 scheme on the same grid. In the case of the exponential and triangular waves, the compact schemes show less clipping at the extrema than the WENO5. The discontinuities in the square wave are less smeared with CRWENO5 and CRWENO5-LD.

While the solutions from the CRWENO5 and CRWENO5-LD schemes were similar after one cycle over the periodic domain, the lower dissipation in the CRWENO5-LD scheme results in better resolution for long-term convection of waves. Figure 4.3 shows the magnified solution around the square and triangular waves after 100 cycles on a grid with 160 points at a CFL of 0.1. The WENO5, CRWENO5, and CRWENO5-LD schemes are compared. The compact schemes perform significantly better than the WENO5 scheme for both waveforms. The difference in the solutions from the CRWENO5 and CRWENO5-LD schemes can be observed, and the CRWENO5-LD shows improved resolution of the square and triangular waves. Figure 4.3(b) shows the computational cost (run-time in seconds) for the various schemes, and it is observed that the compact schemes are more expensive than the WENO5 scheme at the same grid resolution. The solution of the WENO5 scheme on a grid with 240 points is

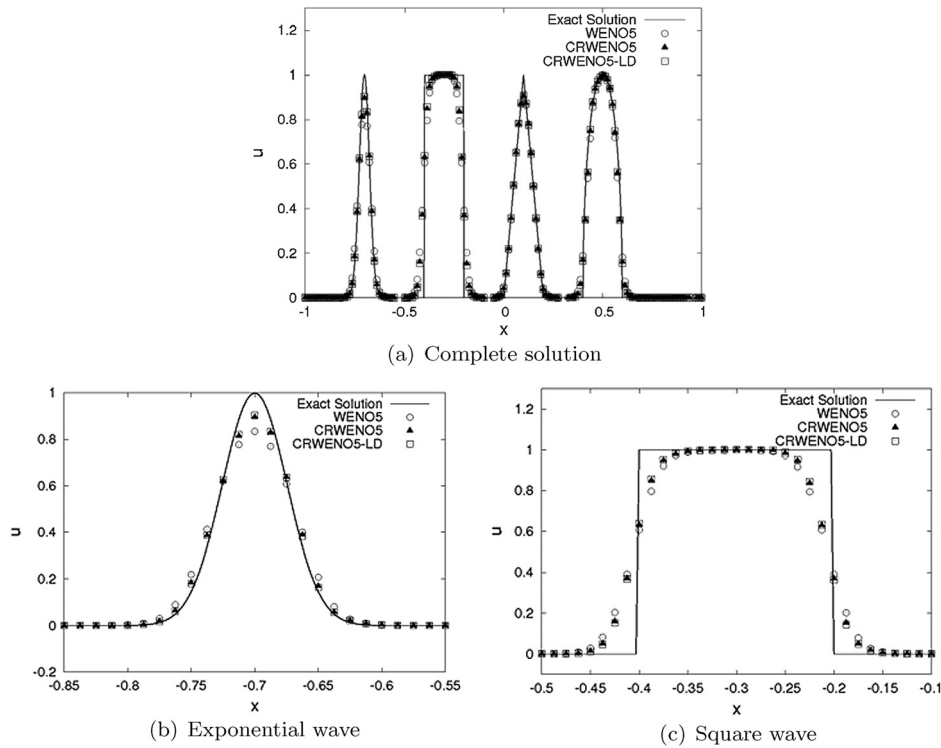


FIG. 4.2. Solution of the linear advection equation after one cycle for discontinuous data on a 160-point grid.

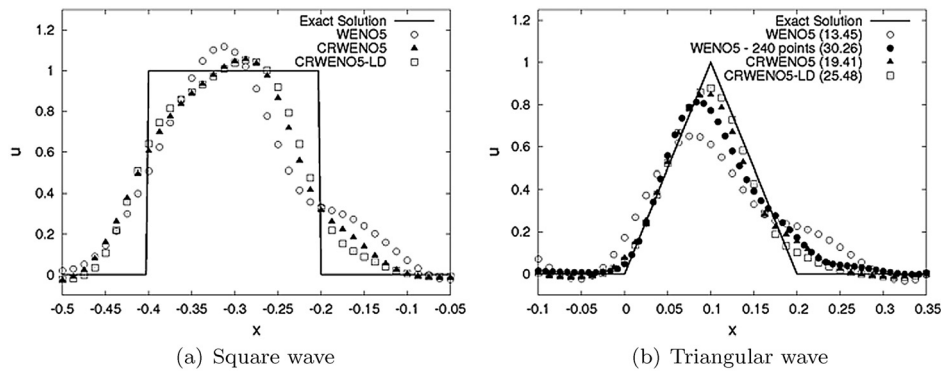


FIG. 4.3. Solution of the linear advection equation after 100 cycles (160-point grid) for discontinuous data (number in parentheses in the legend for the right-hand figure is the run-time in seconds).

included in the figure for comparison. It is observed that the solutions from the compact schemes on a grid with 160 points are comparable with the WENO5 solution on a 240-point grid. As observed previously for the smooth solution, the CRWENO5 and CRWENO5-LD schemes are computationally less expensive when comparing solutions with similar errors.

The two test problems for the linear advection equation demonstrate the properties of the CRWENO schemes. While the scheme achieves its optimal order of

convergence for smooth problems as expected, the absolute value of the errors are lower than the WENO scheme of the same order. Across discontinuities, the CRWENO schemes show an improved resolution compared to the WENO scheme. The lower dissipation and dispersion errors in the compact schemes translate to better capabilities at preserving the waveforms during long-term convection. It should be noted that the long-term convection errors are also sensitive to the choice of weights, and this is an area of active research. Though the compact schemes are costlier than the WENO scheme at the same grid size due to the tridiagonal matrix inversion at each iteration, the lower absolute errors implies that coarser grids may be used to resolve the solution (smooth or discontinuous) to the same accuracy. Thus, the numerical cost of the compact schemes is actually lower with accuracy as the benchmark.

4.2. Inviscid Burgers equation. The inviscid Burgers equation is an example of a scalar nonlinear hyperbolic PDE, given by

$$(4.5) \quad u_t + uu_x = 0.$$

The flux function in (2.1) is thus $f(u) = u^2/2$. The characteristic speed is $f'(u) = u$, and therefore the solution consists of a wave propagating at the local value of u . The shock formation from an initially smooth solution is solved in the present study. The problem provides an initial flow in which the solution is smooth, thus allowing for convergence order estimates. After a certain time, a shock forms in the solution and the nonoscillatory nature of the schemes can be assessed. The initial condition is a sine wave given by

$$(4.6) \quad u_0(x) = \frac{1}{2\pi t_s} \sin(2\pi x),$$

where t_s is a free parameter specifying the time of shock formation ($t_s = 2$ in the present study). Periodic boundary conditions are implemented and the exact solution, prior to shock formation, is defined implicitly as

$$(4.7) \quad u(x, t) = \frac{1}{2\pi t_s} \sin[2\pi(x - u(x, t)t)].$$

An iterative procedure with an initial guess is used to compute the exact solution to machine zero accuracy.

Convergence analysis is done for solutions obtained at $t = 1$, prior to shock formation. The grid is progressively refined from 20 to 640 points. The initial CFL (for the grid with 20 points) is 0.1 and is reduced at each refinement to ensure that time discretization errors converge at the same order as space discretization ones. The L_2 errors are plotted against grid size in Figure 4.4(a) for the WENO5, CRWENO5, and CRWENO5-LD schemes. Errors from the Explicit5, Implicit5, and Implicit5-LD schemes are also plotted for comparison since they should be identical to the WENO schemes for a smooth solution. It is observed that the WENO limiting results in nonoptimal weights at very coarse grids. However, at finer grids, the WENO schemes attain their optimal accuracy, and the errors are identical to the schemes without the limiting. As in the case of the linear advection equation, the CRWENO5 scheme shows significantly lower errors (almost an order of magnitude lower) at all grid resolution, compared to the WENO5 scheme. The CRWENO5-LD scheme has an even lower error (half that of the CRWENO), except on very coarse meshes. Thus, the accuracy and convergence behavior of the compact-reconstruction schemes are thus validated on a nonlinear problem.

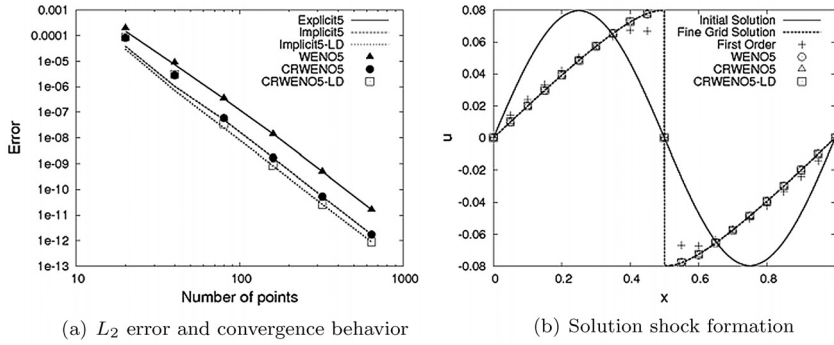


FIG. 4.4. *Inviscid Burgers equation: errors and convergence analysis before shock formation and solution with different schemes after shock formation.*

Figure 4.4(b) shows the solution at $t = 3$ after the formation of a shock on a grid with 20 points for a CFL of 0.5. Solutions obtained using the first order, WENO5, CRWENO5, and CRWENO5-LD schemes are shown. The “fine grid solution” is the solution obtained on a grid of 2000 points with the WENO5 scheme since the exact solution is not available in analytical form. The solutions obtained using the WENO5, CRWENO5, and CRWENO5-LD schemes are seen to be identical for this problem. The nonoscillatory nature of the compact-reconstruction schemes is validated for the nonlinear problem.

5. Extension to the Euler equations of fluid dynamics. The one-dimensional Euler equations can be expressed in the form of a hyperbolic conservation law as

$$(5.1) \quad \mathbf{u}_t + \mathbf{F}_x = 0,$$

where $\mathbf{u} = [\rho \ \rho u \ e]^T$ and $\mathbf{F}(\mathbf{u}) = [\rho u \ (\rho u^2 + p) \ (e + p)u]^T$. The fluid density is ρ , the pressure is p , and velocity is u . The equation of state relates the internal energy e to the flow variables [2]. The two-dimensional Euler equations can be similarly expressed. The discretization described in section 2 can be extended to the system of equations. The TVDRK3 scheme is used for time marching with high order spatial schemes.

The discretization described above requires the approximation of the numerical flux function $\hat{\mathbf{F}}_{j+1/2}$, which is a vector quantity, at the interfaces. The previous sections described the interpolation of a scalar quantity using the WENO and CRWENO family of schemes. These schemes can be applied to the Euler system in two possible ways. The scalar interpolation can be applied individually to each component of the vector flux function, and this will be referred to as the conserved variable reconstruction (as an alternative, the primitive flow variables, ρ, u, p , can be reconstructed at each interface and the interface flux then calculated). The extension of the scalar interpolation schemes to the reconstruction of conserved (and primitive) variables is trivial.

The hyperbolicity of the Euler equations implies that the solution is composed of waves. The characteristic speeds and directions of these waves are given by the eigenvalues and eigenvectors of the flux Jacobian matrix. The conserved variable reconstruction computes the left and right biased interface fluxes ($\hat{\mathbf{F}}_{j+1/2}^L, \hat{\mathbf{F}}_{j+1/2}^R$), and the Roe flux differencing [41] is used to find the upwind interface flux, expressed as

$$(5.2) \quad \hat{\mathbf{F}}_{j+1/2} = \frac{1}{2}(\hat{\mathbf{F}}_{j+1/2}^L + \hat{\mathbf{F}}_{j+1/2}^R) - \frac{1}{2}|\hat{A}(\hat{\mathbf{U}}_{j+1/2}^L, \hat{\mathbf{U}}_{j+1/2}^R)|(\hat{\mathbf{U}}_{j+1/2}^L - \hat{\mathbf{U}}_{j+1/2}^R),$$

where \hat{A} is the Roe-averaged Jacobian matrix. $\hat{\mathbf{U}}_{j+1/2}^{L,R}$ are the left and right biased reconstructed values of \mathbf{U} at the interface.

The third approach—reconstruction of the characteristic variables—is physically more robust than the other two [3, 8]. The wave nature of the solution implies that along each characteristic the solution is similar to a scalar wave propagation, and thus application of the scalar interpolation techniques to the characteristic variables is physically more accurate. At interface $x_{i+1/2}$, the Roe-averaged Jacobian matrix, $\hat{A}(\mathbf{U}_i, \mathbf{U}_{i+1})$, yields the eigenvalues ($\lambda_{i+1/2}^k$), left eigenvectors ($\mathbf{l}_{i+1/2}^k$), and right eigenvectors ($\mathbf{r}_{i+1/2}^k$) which define the wave structure at that interface, where k is the index denoting each characteristic field. The k th characteristic flux at the j th cell is the component of the flux vector along the k th left eigenvector at the $i + 1/2$ th interface and can be expressed as

$$(5.3) \quad \alpha_j^k = \mathbf{l}_{i+1/2}^k \cdot \mathbf{F}(x_j).$$

Equation (3.17) is applied to the characteristic fluxes to compute the left biased WENO5 approximation of the k th characteristic flux at the interface,

$$(5.4) \quad \begin{aligned} \hat{\alpha}_{j+1/2}^{L,k} &= \frac{\omega_1}{3} \alpha_{j-2}^k - \frac{1}{6} (7\omega_1 + \omega_2) \alpha_{j-1}^k + \frac{1}{6} (11\omega_1 + 5\omega_2 + 2\omega_3) \alpha_j^k \\ &+ \frac{1}{6} (2\omega_2 + 5\omega_3) \alpha_{j+1}^k - \frac{\omega_3}{6} \alpha_{j+2}^k. \end{aligned}$$

The right biased characteristic flux, $\hat{\alpha}^{R,k}$, can be similarly computed. Applying (3.24) or (3.27) to the characteristic fluxes, we get the general form of the CRWENO5 or CRWENO5-LD scheme in its characteristic form as

$$(5.5) \quad a \hat{\alpha}_{j-1/2}^{L,k} + b \hat{\alpha}_{j+1/2}^{L,k} + c \hat{\alpha}_{j+3/2}^{L,k} = \hat{a} \alpha_{j-1}^k + \hat{b} \alpha_j^k + \hat{c} \alpha_{j+1}^k + \hat{d} \alpha_{j+2}^k,$$

where $a, b, c, \hat{a}, \hat{b}, \hat{c}, \hat{d}$ are the appropriate coefficients. Using (5.3) to expand the characteristic fluxes in the above equation, we get a system of equation expressed as

$$(5.6) \quad \begin{aligned} &a(l_{k1} \hat{F}_{1,j-1/2}^L + l_{k2} \hat{F}_{2,j-1/2}^L + l_{k3} \hat{F}_{3,j-1/2}^L) + b(l_{k1} \hat{F}_{1,j+1/2}^L + l_{k2} \hat{F}_{2,j+1/2}^L + l_{k3} \hat{F}_{3,j+1/2}^L) \\ &= \hat{a} \alpha_{j-1}^k + \hat{b} \alpha_j^k + \hat{c} \alpha_{j+1}^k + \hat{d} \alpha_{j+2}^k + c(l_{k1} \hat{F}_{1,j+3/2}^L + l_{k2} \hat{F}_{2,j+3/2}^L + l_{k3} \hat{F}_{3,j+3/2}^L), \end{aligned}$$

where l_{k1}, l_{k2}, l_{k3} are the components of the left eigenvector $\mathbf{l}_{j+1/2}^k$ and $\hat{F}_{1,j+1/2}^L, \hat{F}_{2,j+1/2}^L$, and $\hat{F}_{3,j+1/2}^L$ are the components of the flux vector $\hat{\mathbf{F}}_{j+1/2}^L$. The one-dimensional system of equations has three characteristic fields ($k = 1, 2, 3$), and (5.6) results in a 3×3 block tridiagonal system. The two- and three-dimensional Euler equations would require the inversion of 4×4 and 5×5 block tridiagonal systems, respectively. The right biased numerical fluxes can be computed in a similar fashion.

The Roe-fixed (RF) formulation [5, 6] is used to compute the upwind characteristic flux from the left and right biased approximations. It incorporates the local Lax–Friedrich flux splitting [42] as an entropy fix to the Roe solver [41]. It can be expressed as

$$(5.7) \quad \hat{\alpha}_{j+1/2}^k = \begin{cases} \hat{\alpha}_{j+1/2}^{L,k} & \text{if } \lambda_{j,j+1/2,j+1} > 0, \\ \hat{\alpha}_{j+1/2}^{R,k} & \text{if } \lambda_{j,j+1/2,j+1} < 0, \\ \frac{1}{2} \left[\hat{\alpha}_{j+1/2}^{L,k} + \hat{\alpha}_{j+1/2}^{R,k} + \tilde{\lambda} (\hat{v}_{j+1/2}^{L,k} - \hat{v}_{j+1/2}^{R,k}) \right] & \text{otherwise,} \end{cases}$$

where $\tilde{\lambda} = \mu \lambda_{\max}[j, j + 1/2, j + 1]$ and $v_j^k = \mathbf{I}_{i+1/2}^k \cdot \mathbf{U}(x_j)$ is the characteristic state vector. The dissipation parameter, μ , is usually between 1.1 and 1.3.

The two approaches of extending the scalar interpolation schemes to the system of equations are compared in the present study for smooth problems as well as problems with discontinuities. The characteristic reconstruction process is computationally more expensive than the conserved (or primitive) variables reconstruction processes. While the difference in computational cost is marginal for the WENO5 scheme, it is significant for the CRWENO5 and CRWENO5-LD schemes where the characteristic-based reconstruction requires the inversion of a block tridiagonal system instead of a tridiagonal system. The conserved variable reconstruction performs well for smooth problems; however, a characteristic-based reconstruction is required to yield nonoscillatory solutions for flows with shock waves and contact discontinuities. The description in this section for the one-dimensional Euler equations can be extended to two- and three-dimensional systems.

6. Numerical results: Euler equations. The compact schemes described in the previous section are applied to one-dimensional and two-dimensional inviscid flow problems. The accuracy and convergence properties are analyzed for the advection of an entropy wave, which is a smooth problem with an exact analytical solution. A one-dimensional Riemann problem is solved to validate the nonoscillatory nature of the schemes. The characteristic- and conserved variables-based reconstruction algorithms are compared for these problems since they require a robust solution algorithm to yield nonoscillatory solutions. Finally, the shock entropy wave interaction problem is studied since the solution comprises discontinuities as well as high-frequency waves. The performance of the schemes is analyzed for the convection of an isentropic vortex over a periodic domain, especially for long-term convection. The double Mach reflection of a strong shock is solved to validate the schemes for a two-dimensional flow with strong discontinuities. Finally, the interaction of a shock wave with an isentropic vortex is simulated since this provides a flow with discontinuous and smooth structures.

6.1. Entropy wave advection. The problem simulates the advection of a density wave at a constant freestream velocity while pressure and velocity remain constant. The solution at any time is given by

$$(6.1) \quad \rho(x, t) = \rho_{\infty} + A \sin[\pi(x - u_{\infty}t)]; \quad u(x, t) = u_{\infty}; \quad p(x, t) = p_{\infty}.$$

The freestream conditions are taken as $\rho_{\infty} = u_{\infty} = p_{\infty} = 1$, and the amplitude of the density wave is taken as $A = 0.1$. The domain is $[0, 2]$ and discretized with a uniform grid. Periodic boundary conditions are enforced at both boundaries. The solution is obtained after one cycle at $t = 2$ and the errors calculated.

The problem is solved using the WENO5, CRWENO5, and CRWENO5-LD schemes. Figure 6.1(a) shows the L_2 norm of the error as a function of grid size for the three schemes and their optimal counterparts using the conserved variable reconstruction. An initial grid of 15 points is refined successively and the CFL (for the grid of 15 points) is 0.1. The compact schemes show significantly lower error for the same order of convergence. Figure 6.1(b) compares the errors for the conserved and characteristic variables reconstructions for the WENO5, CRWENO5, and CRWENO5-LD schemes. It is observed that for a smooth problem, the two reconstructions give identical solutions (it should be noted here that this flow problem reduces the nonlinear Euler equations to a linear advection equation for the density). Tables 6.1 and 6.2

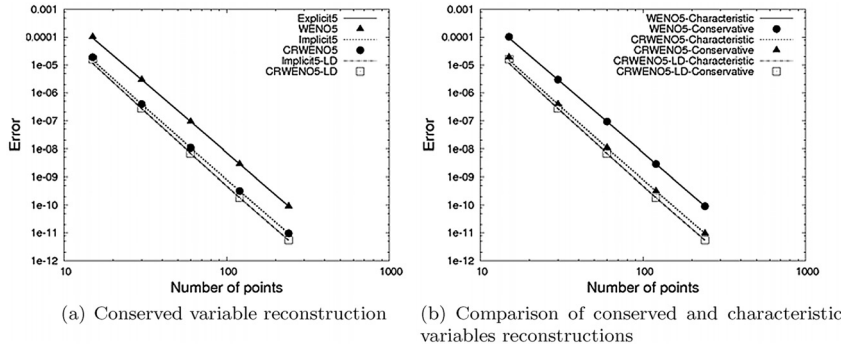


FIG. 6.1. L_2 error norm vs. grid size of entropy wave advection.

TABLE 6.1

L_2 errors and convergence rates for *Explicit5*, *Implicit5*, and *Implicit5-LD* for entropy wave advection.

N	Explicit5		Implicit5		Implicit5-LD	
	Error	r_c	Error	r_c	Error	r_c
15	9.293E-05	-	1.483E-05	-	1.141E-05	-
30	2.967E-06	4.97	3.877E-07	5.26	2.717E-07	5.39
60	9.321E-08	4.99	1.083E-08	5.16	6.854E-09	5.31
120	2.916E-09	5.00	3.172E-10	5.09	1.843E-10	5.22
240	9.097E-11	5.00	9.598E-12	5.05	5.472E-12	5.07

TABLE 6.2

L_2 errors and convergence rates for *WENO5*, *CRWENO5*, and *CRWENO5-LD* for entropy wave advection.

N	WENO5		CRWENO5		CRWENO5-LD	
	Error	r_c	Error	r_c	Error	r_c
15	1.028E-04	-	1.900E-05	-	1.598E-05	-
30	2.988E-06	5.10	3.946E-07	5.59	2.759E-07	5.86
60	9.325E-08	5.00	1.084E-08	5.19	6.860E-09	5.33
120	2.917E-09	5.00	3.172E-10	5.10	1.843E-10	5.22
240	9.098E-11	5.00	9.599E-12	5.05	5.470E-12	5.07

show the L_2 errors (density) and orders of convergence for the three schemes (and their optimal counterparts) with conserved variable reconstruction. While there are some irregularities in the errors and convergence orders at very coarse grids (between the WENO and optimal schemes), the errors are identical as the grids are refined (as expected for a smooth problem). The errors for the CRWENO5 and CRWENO5-LD schemes are an order of magnitude lower than the WENO5 scheme. At finer grid resolutions, the L_2 errors for CRWENO5-LD are almost half those of CRWENO5.

The numerical cost of the compact schemes is evaluated for the one-dimensional Euler equations. Table 6.3 shows the L_2 errors and the run-time (in seconds) for the WENO5, CRWENO5, and CRWENO5-LD schemes at different grid resolutions for solutions obtained after 10 cycles over the periodic domain. The conserved variable reconstruction is used. The CFL corresponding to the initial grid of 30 points is 0.1 and is reduced for finer grids to maintain fifth order accuracy. The observations are similar to those for the linear advection equation for the conserved variable reconstruction since it is equivalent to three scalar compact reconstructions, involving the inversion of a tridiagonal matrix. The computational expense of the compact

TABLE 6.3

L_2 errors and computational run-time (in seconds) for WENO5, CRWENO5, and CRWENO5-LD for entropy wave advection with conserved variable reconstruction.

N	WENO5		CRWENO5		CRWENO5-LD	
	Error	T	Error	T	Error	T
30	2.999E-05	1.01	3.823E-06	1.33	2.230E-06	1.62
45	3.967E-06	2.29	-	-	-	-
60	9.359E-07	6.27	1.076E-07	8.29	5.976E-08	10.30
90	1.241E-07	14.37	-	-	-	-
120	2.928E-08	39.13	3.209E-09	51.63	1.733E-09	66.10
180	3.879E-09	90.25	-	-	-	-
240	9.136E-10	258.23	9.723E-11	329.54	5.222E-11	399.04
360	1.204E-10	576.41	-	-	-	-

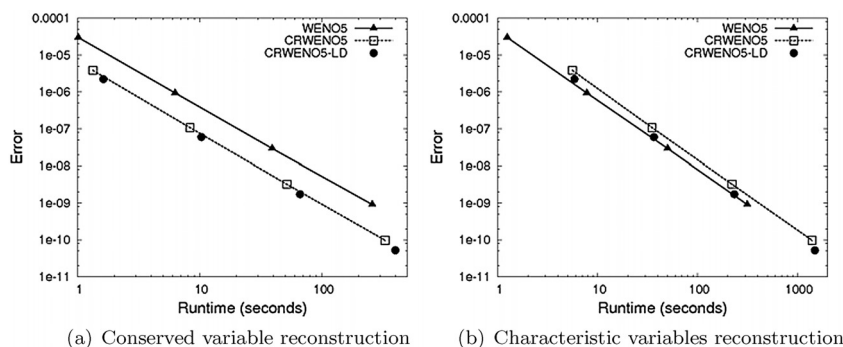


FIG. 6.2. Numerical cost of different schemes with conserved and characteristic variable reconstructions.

schemes is higher at the same grid resolution. However, the compact schemes yield lower errors, and thus comparing the computational cost of solutions which have the same absolute error, shows that the compact schemes are actually less expensive. The numerical error of the compact schemes on grids with 30, 60, 120, and 240 points are comparable to that of the WENO5 scheme on grids with 45, 90, 180, and 360 points, respectively, while the computational expense is significantly lower. Figure 6.2(a) shows the L_2 error as a function of the numerical cost for the three schemes, and it is observed that the CRWENO5 and CRWENO5-LD schemes are less expensive than the WENO5 scheme for solutions with the same error.

Table 6.4 shows the L_2 errors and the run-time for the schemes with characteristic-based reconstruction. The characteristic variables formulation of the compact schemes

TABLE 6.4

L_2 errors and computational run-time (in seconds) for WENO5, CRWENO5, and CRWENO5-LD for entropy wave advection with characteristic-based reconstruction.

N	WENO5		CRWENO5		CRWENO5-LD	
	Error	T	Error	T	Error	T
30	2.998E-05	1.24	3.824E-06	5.58	2.229E-06	5.85
45	3.967E-06	2.81	-	-	-	-
60	9.359E-07	7.78	1.076E-07	34.97	5.976E-08	36.57
90	1.241E-07	17.61	-	-	-	-
120	2.928E-08	50.11	3.209E-09	221.75	1.733E-09	233.67
180	3.879E-09	110.92	-	-	-	-
240	9.136E-10	314.19	9.722E-11	1405.66	5.223E-11	1498.15
360	1.204E-10	702.10	-	-	-	-

requires the inversion of a block tridiagonal matrix, and thus the computational expense is significantly larger. This is observed in the table where the run-times of the CRWENO5 and CRWENO5-LD schemes are significantly higher than those of the WENO5 scheme at the same grid resolution. The numerical cost is compared for solutions with similar absolute errors which are obtained by the WENO5 scheme on finer grids with 1.5 times the number of points. The CRWENO5 and CRWENO5-LD schemes, in their characteristic formulation, are observed to be more expensive for the same accuracy, and thus less efficient. Figure 6.2(b) shows the L_2 error as a function of the numerical cost for the three schemes with characteristic-based reconstruction. At the same value of error, the CRWENO5 scheme is more expensive, but CRWENO5-LD is observed to be as efficient as WENO5.

6.2. Shock entropy wave interaction. The interaction of a shock wave with a density wave [5] is simulated in this problem. The initial conditions, which consist of a Mach 3 shock wave interacting with a density wave, are given by [38]

$$\begin{aligned}
 (\rho, u, p) &= \left(\frac{27}{7}, \frac{4\sqrt{35}}{9}, \frac{31}{3} \right) \text{ if } x < -4 \\
 &= \left(1 + \frac{1}{5} \sin 5x, 0, 1 \right) \text{ if } x \geq -4.
 \end{aligned}
 \tag{6.2}$$

The domain is taken as $[-5, 5]$ and zero-gradient boundaries are applied at both boundaries. The solution is obtained at $t = 1.8$ at a CFL of 0.1. Figure 6.3(a) shows the density on a grid with 200 points for the WENO5, CRWENO5, and CRWENO5-LD schemes using a characteristic-based reconstruction. Figure 6.3(b) shows the same solution, magnified around the postshock high-frequency waves. “Fine Grid Solution” refers to the solution obtained by the WENO5 scheme on a grid with 2000 points and is used as the reference solution in absence of an exact one. It is observed that the compact schemes show significant improvement in resolving the high-frequency waves while maintaining nonoscillatory behavior across the shock waves. In addition, the compact schemes show significantly lower smearing for the shock wave. Thus, the improved performance due to the use of compact interpolations is validated on a problem with discontinuities as well as high-frequency smooth waves. The characteristic formulation of the compact schemes was shown to be computationally less efficient in the previous section, and these results are intended to demonstrate the improved resolution of the new schemes. It is well known that the reconstruction

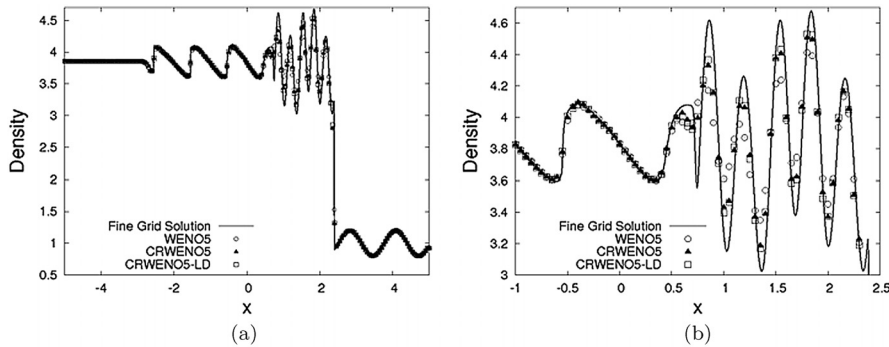


FIG. 6.3. Interaction of a shock wave with a density wave.

of conserved or primitive variables yield oscillatory solutions for inviscid flows with strong discontinuities, and thus a characteristic-based algorithm is necessary.

6.3. Isentropic vortex convection. The convection of an isentropic vortex [6] with the freestream flow is simulated. In the present study, the domain is $[0, 10] \times [0, 10]$ with freestream flow as $\rho_\infty = 1, u_\infty = 0.5, v_\infty = 0, p_\infty = 1$. A vortex is introduced in the flow, initially centered at $(x_c, y_c) = (5, 5)$, specified as

$$(6.3) \quad \begin{aligned} \rho &= \left[1 - \frac{(\gamma - 1)b^2}{8\gamma\pi^2} e^{1-r^2} \right]^{\frac{1}{\gamma-1}}; \quad p = \rho^\gamma, \\ \delta u &= -\frac{b}{2\pi} e^{\frac{1-r^2}{2}} (y - y_c), \\ \delta v &= \frac{b}{2\pi} e^{\frac{1-r^2}{2}} (x - y_c), \end{aligned}$$

where $r = ((x - x_c)^2 + (y - y_c)^2)^{1/2}$ is the distance from the vortex center and $b = 0.5$ is the vortex strength. Periodic boundary conditions are applied at all boundaries. As the solution is evolved in time, the vortex convects over the periodic domain with a time period of $T_p = 20$.

The behavior of the schemes for long-term convection of the vortex is assessed for a convection distance of 1000 core radii. Figures 6.4(a)–6.4(d) show the density contours for the initial vortex and the solutions obtained by the WENO5, CRWENO5, and CRWENO5-LD schemes on a 60×60 grid. The conserved variables are reconstructed since the problem is smooth and lacks any discontinuities. The compact schemes show significant improvement in preserving the vortex shape and strength as it convects over large distances. Figure 6.4(e) shows the absolute error (nondimensionalized) in minimum pressure at the vortex core as it convects, for the three schemes. The low numerical dissipation in the compact schemes results in maintaining the density minimum at the vortex core, as compared to the WENO5 scheme. The cross-sectional pressure profiles through the vortex, core are shown in Figure 6.4(f). The compact schemes are observed to retain the original shape and strength of the vortex, while the solution obtained using WENO5 shows substantial dissipation and distortion.

The computational expense of the compact schemes is studied for this two-dimensional problem. The legend of Figure 6.4(e) shows the run-time (in seconds) per time period T_p of the three schemes. The error in pressure and the cross-sectional pressure profile for the WENO5 scheme on a 90×90 grid is also included for comparison in Figures 6.4(e) and 6.4(f), respectively. The compact schemes are costlier than the WENO5 scheme at the same grid size. However, their resolution of the solution is comparable to the WENO5 scheme on the finer grid, and they are substantially less expensive when solutions with similar resolution are compared. These observations are consistent with those for the linear advection equation and the one-dimensional entropy wave advection case; however, the reduction in computational expense is amplified for the two-dimensional problem. The CRWENO5 and CRWENO5-LD schemes on a 60×60 grid resolve the vortex to the same accuracy as the WENO5 scheme on a 90×90 grid at less than half the run-time.

6.4. Double mach reflection of a strong shock. The reflection of a strong shock from an inviscid wall [43] is simulated in this problem and provides a validation of the algorithm for a problem with wave reflection at solid boundaries. The domain is $[0, 4] \times [0, 1]$ and the initial condition consists of a Mach 10 shock intersecting the bottom boundary $y = 0$ at $x = \frac{1}{6}$ and making an angle of 60° to the x-axis. The flow

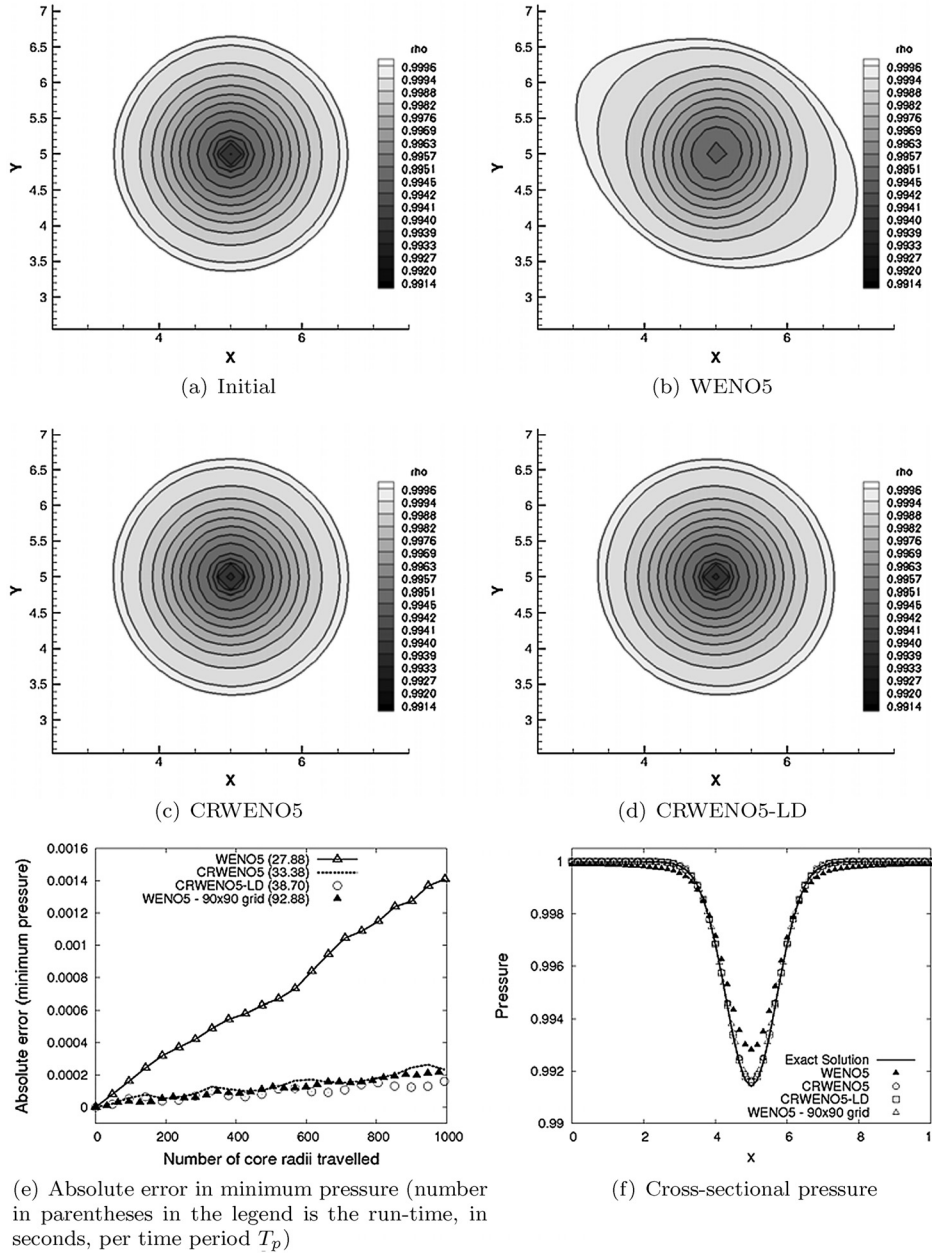


FIG. 6.4. Density contours after traveling 1000 core radii and vortex core pressure with different schemes on a 60×60 grid.

to the right of the shock is initialized as $(\rho, u, v, p) = (1.4, 0, 0, 1)$, while postshock flow conditions are specified to the left. The right and left boundaries are set to the pre- and postshocked flow values. At the bottom boundary, inviscid wall boundary conditions are imposed on $\frac{1}{6} < x < 4$, while postshock flow conditions are applied for $x < \frac{1}{6}$. Boundary conditions on the top boundary correspond to the exact motion of a Mach 10 shock.

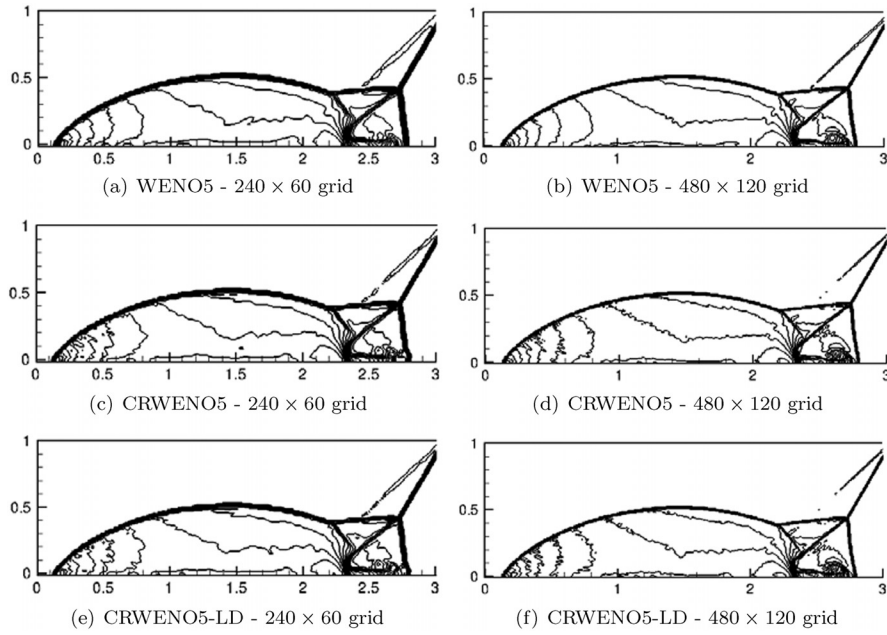


FIG. 6.5. *Density contours of the double Mach reflection problem with different schemes.*

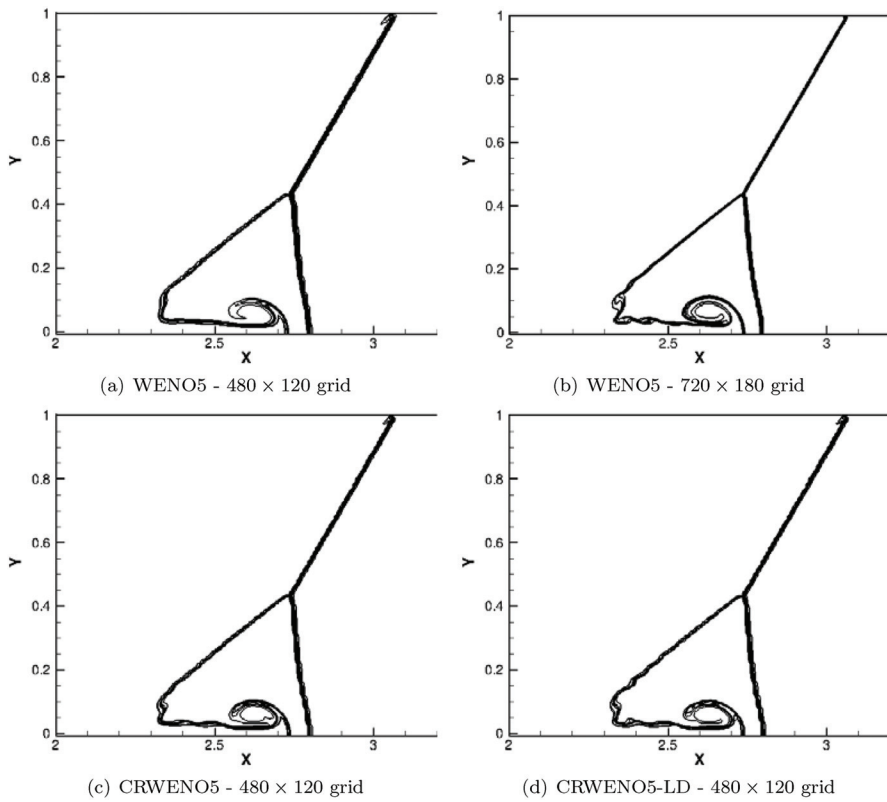


FIG. 6.6. *Entropy contours of the double Mach reflection problem with different schemes.*

The problem is solved on a uniform grid with 240×60 and 480×120 points with CFL values of 0.6 and 0.1, respectively. Characteristic reconstruction is used since the flow is composed of strong incident and reflected shocks. Figure 6.5 shows the density contours obtained by the WENO5, CRWENO5, and CRWENO5-LD schemes at $t = 0.2$. The figures on the left-hand side show the solutions obtained on the coarse grid, while the figures on the right show the solutions obtained on a fine grid. Thirty contours are plotted from 1.731 to 20.92 for all three solutions. It is observed that the shocks and the Mach stems are well captured at our grid resolutions with all three schemes and compare well with the solutions presented in the literature [8, 9], including those obtained with finer grids. The solutions obtained using the CRWENO5 and CRWENO5-LD schemes show more oscillations due to the reduced dissipation. However, the shocks are visibly less smeared with the compact schemes. Figure 6.6 shows the entropy contours for the solutions obtained on the fine grid. The compact schemes show an improved resolution of the contact discontinuity roll-up at the base of the Mach stem. The solution obtained with the WENO5 scheme on a 720×180 grid is shown for comparison. It is observed that the resolution of the solution obtained by the CRWENO5 and CRWENO5-LD schemes on the 480×120 grid is comparable to that of the WENO5 solution on the finer grid. The resolution of our fifth order compact schemes is comparable to that of the ninth order MPWENO of Balsara and Shu [9] (see Figure 7(b) on page 445).

7. Conclusion. A class of compact-reconstruction WENO (CRWENO) schemes is presented in this paper. Our objective is to increase the accuracy and spectral properties of the WENO schemes of Jiang and Shu for a given order of convergence. At each interface, lower order candidate compact stencils are identified and optimal coefficients are found such that a weighted combination of these stencils yields a higher order compact stencil. The optimal weights are modified based on the smoothness of the corresponding stencil such that the final compact scheme is high order accurate in smooth regions of the solution and maintain nonoscillatory behavior at or near discontinuities. A low-dissipation variant of the CRWENO scheme is also presented where an additional point is included in the stencil to reduce dissipation, while maintaining the upwind nature of the reconstruction. The new schemes have lower Taylor series errors and higher bandwidth resolving efficiencies for the same order of convergence.

The new schemes are validated and their performance is analyzed for scalar conservation laws. The accuracy and resolution of the new schemes are shown to be superior to the WENO schemes for both smooth and discontinuous solutions. A tridiagonal matrix inversion is required at each iteration because the implicit system resulting from our compact schemes is solution-dependent. This introduces a significant computational overhead. However, it is shown through numerical tests that the improved accuracy of the schemes allows the use of coarser meshes to achieve the same resolution of the solution as the corresponding WENO scheme. Thus, the new schemes are computationally more efficient than the WENO schemes of Jiang and Shu.

The compact schemes are extended to the Euler equations of fluid dynamics. It is well known that while the reconstruction of conserved variables suffices for smooth flows, a characteristic-based reconstruction is necessary to yield nonoscillatory results for flows with strong discontinuities. Our schemes extend trivially to the reconstruction of conserved variables, and our observations for the scalar conservation laws are reiterated for the Euler system with smooth solutions. The increase in computational efficiency is amplified in two dimensions. The computational overhead of a tridiagonal matrix inversion is balanced by the significant increase in accuracy and resolution.

The implementation of our compact schemes in the characteristic space is described. The characteristic-based CRWENO schemes are observed to be robust and yield nonoscillatory solutions for flows with strong discontinuities. The improved resolution is demonstrated for both the one-dimensional and two-dimensional Euler equations. However, the reconstruction of characteristic variables with our compact schemes requires a block tridiagonal inversion at each iteration. A multidimensional domain requires the block tridiagonal inversion along each grid line of each dimension. The numerical cost of these operations is significant, and the computational efficiency of the characteristic formulation is lower than that of the noncompact WENO schemes. The application of the characteristic-based CRWENO schemes to inviscid flow problems may be impractical. However, this may not be an impediment to the application of the schemes to the Navier–Stokes equations and to larger, real-world flow problems. The fraction of the numerical cost for the reconstruction step is lower for algorithms used in such applications, that solve viscous, turbulent flows on curvilinear or unstructured meshes, often with implicit time marching. Thus, the computational overhead of the CRWENO schemes may not be significant and the higher resolution obtained may justify the cost.

It is also known that while the characteristic-based reconstruction is necessary for inviscid flow problems with strong discontinuities, reconstruction of conserved or primitive variables suffices when physical viscosity is present. The resolution and computational efficiency of the CRWENO schemes with conserved variable reconstruction has been demonstrated and indicate their suitability for simulating flows with a large range of length scale (e.g., direct numerical simulation of turbulence) and simulation of flows involving long-term convection of vortical structures (e.g., rotorcraft wake flows). The application of the CRWENO schemes to the two- and three-dimensional Navier–Stokes equations for the simulation of such flows will be discussed in future studies.

REFERENCES

- [1] R. J. LEVEQUE, *Finite Volume Methods for Hyperbolic Problems*, Cambridge University Press, Cambridge, UK, 2002.
- [2] C. B. LANEY, *Computational Gasdynamics*, Cambridge University Press, Cambridge, UK, 1998.
- [3] A. HARTEN, B. ENQUIST, S. OSHER, AND S. CHAKRAVARTHY, *Uniformly high order essentially non oscillatory schemes*, III, *J. Comput. Phys.*, 71 (1987), pp. 231–303.
- [4] C.-W. SHU AND S. OSHER, *Efficient implementation of essentially non-oscillatory schemes*, *J. Comput. Phys.*, 77 (1988), pp. 439–471.
- [5] C.-W. SHU AND S. OSHER, *Efficient implementation of essentially non-oscillatory schemes*, II, *J. Comput. Phys.*, 83 (1989), pp. 32–78.
- [6] C.-W. SHU, *Essentially Non-oscillatory and Weighted Essentially Non-oscillatory Schemes for Hyperbolic Conservation Laws*, ICASE Report 97-65, 1997.
- [7] X. LIU, S. OSHER, AND T. CHAN, *Weighted essentially non-oscillatory schemes*, *J. Comput. Phys.*, 115 (1994), pp. 200–212.
- [8] G.-S. JIANG AND C.-W. SHU, *Efficient implementation of weighted ENO schemes*, *J. Comput. Phys.*, 126 (1996), pp. 202–228.
- [9] D. S. BALSARA, AND C.-W. SHU, *Monotonicity preserving weighted essentially non-oscillatory schemes with increasingly high order of accuracy*, *J. Comput. Phys.*, 160 (2000), pp. 405–452.
- [10] S. K. LELE, *Compact finite difference schemes with spectral-like resolution*, *J. Comput. Phys.*, 103 (1992), pp. 16–42.
- [11] W. E AND J. G. LIU, *Essentially compact schemes for unsteady viscous incompressible flows*, *J. Comput. Phys.*, 126 (1996), pp. 122–138.
- [12] R. V. WILSON, A. Q. DEMUREN, AND M. H. CARPENTER, *High-Order Compact Schemes for Numerical Simulation of Incompressible Flows*, ICASE Report 98-13, 1998.

- [13] A. LERAT AND C. CORRE, *A residual-based compact scheme for the compressible Navier-Stokes equations*, J. Comput. Phys., 170 (2001), pp. 642–675.
- [14] J. A. EKATERINARIS, *Implicit, high-resolution compact schemes for gas dynamics and aeroacoustics*, J. Comput. Phys., 156 (1999), pp. 272–299.
- [15] T. K. SENGUPTA, G. GANERIWAL, AND S. DE, *Analysis of central and upwind compact schemes*, J. Comput. Phys., 192 (2003), pp. 677–694.
- [16] J. S. SHANG, *High-order compact-difference schemes for time-dependent Maxwell equations*, J. Comput. Phys., 153 (1999), pp. 312–333.
- [17] C. LEE AND Y. SEO, *A new compact spectral scheme for turbulence simulations*, J. Comput. Phys., 183 (2002), pp. 438–469.
- [18] K. MAHESH, S. K. LELE, AND P. MOIN, *The influence of entropy fluctuations on the interaction of turbulence with a shock wave*, J. Fluid Mech., 334 (1997), pp. 353–379.
- [19] S. NAGARAJAN, S. K. LELE, AND J. H. FERZIGER, *A robust high-order compact method for large eddy simulation*, J. Comput. Phys., 191 (2003), pp. 392–419.
- [20] D. GAITONDE AND J. S. SHANG, *Optimized compact-difference-based finite volume schemes for linear wave phenomena*, J. Comput. Phys., 138 (1997), pp. 617–643.
- [21] M. H. KOBAYASHI, *On a class of Padé finite volume methods*, J. Comput. Phys., 156 (1999), pp. 137–180.
- [22] L. GAMET, F. DUCROS, F. NICOUD, AND T. POINSOT, *Compact finite difference schemes on non-uniform meshes. Application to direct numerical simulations of compressible flows*, Internat. J. Numer. Methods Fluids, 29 (1999), pp. 159–191.
- [23] M. R. VISBAL AND D. V. GAITONDE, *On the use of higher-order finite-difference schemes on curvilinear and deforming meshes*, J. Comput. Phys., 181 (2001), pp. 155–185.
- [24] R. K. SHUKLA AND X. ZHONG, *Derivation of high-order compact finite difference schemes for non-uniform grid using polynomial interpolation*, J. Comput. Phys., 204 (2005), pp. 404–429.
- [25] B. COCKBURN AND C.-W. SHU, *Nonlinearly stable compact schemes for shock calculations*, SIAM J. Numer. Anal., 31 (1994), pp. 607–627.
- [26] H. C. YEE, *Explicit and implicit multidimensional compact high-resolution shock-capturing methods: Formulation*, J. Comput. Phys., 131 (1997), pp. 216–232.
- [27] N. A. ADAMS AND K. SHARIFF, *A high-resolution hybrid compact-ENO scheme for shock-turbulence interaction problems*, J. Comput. Phys., 127 (1996), pp. 27–51.
- [28] N. A. ADAMS, *Direct numerical simulation of turbulent compression ramp flow*, Theor. Comput. Fluid Dyn., 12 (1998), pp. 109–129.
- [29] S. PIROZZOLI, *Conservative hybrid compact-WENO schemes for shock-turbulence interaction*, J. Comput. Phys., 178 (2002), pp. 81–117.
- [30] Y.-X. REN, M. LIU, AND H. ZHANG, *A characteristic-wise hybrid compact-WENO scheme for solving hyperbolic conservation laws*, J. Comput. Phys., 192 (2003), pp. 365–386.
- [31] X. DENG AND H. MAEKAWA, *Compact high-order accurate nonlinear schemes*, J. Comput. Phys., 130 (1997), pp. 77–91.
- [32] X. DENG AND H. ZHANG, *Developing high order weighted compact nonlinear schemes*, J. Comput. Phys., 165 (2000), pp. 22–44.
- [33] S. ZHANG, S. JIANG, AND C.-W. SHU, *Development of nonlinear weighted compact schemes with increasingly higher order accuracy*, J. Comput. Phys., 227 (2008), pp. 7294–7321.
- [34] Z. WANG AND G. P. HUANG, *An essentially nonoscillatory high order Padé-type (ENO-Padé) scheme*, J. Comput. Phys., 177 (2002), pp. 37–58.
- [35] D. LEVY, G. PUPPO, AND G. RUSSO, *Compact central WENO schemes for multidimensional conservation laws*, SIAM J. Sci. Comput., 22 (2000), pp. 656–672.
- [36] L. JIANG, H. SHAN, AND C. Q. LIU, *Weighted compact scheme for shock capturing*, Int. J. Comput. Fluid Dyn., 15 (2001), pp. 147–155.
- [37] M. P. MARTIN, E. M. TAYLOR, M. WU, AND V. G. WEIRS, *A bandwidth-optimized WENO scheme for the effective direct numerical simulation of compressible turbulence*, J. Comput. Phys., 220 (2006), pp. 270–289.
- [38] A. K. HENRICK, T. D. ASLAM, AND J. M. POWERS, *Mapped weighted essentially non-oscillatory schemes: Achieving optimal order near critical points*, J. Comput. Phys., 207 (2005), pp. 542–567.
- [39] R. BORGES, M. CARMONA, B. COSTA, AND W. S. DON, *An improved weighted essentially non-oscillatory scheme for hyperbolic conservation laws*, J. Comput. Phys., 227 (2008), pp. 3191–3211.
- [40] N. K. YAMALEEV AND M. H. CARPENTER, *A systematic methodology for constructing high-order energy stable WENO schemes*, J. Comput. Phys., 228 (2009), pp. 4248–4272.

- [41] P. ROE, *Approximate Riemann solvers, parameter vectors and difference schemes*, J. Comput. Phys., 135 (1997), pp. 250–258.
- [42] P. D. LAX, *Weak solutions of nonlinear hyperbolic equations and their numerical computation*, Comm. Pure Appl. Math., 7 (1954), pp. 159–193.
- [43] P. WOODWARD, AND P. COLELLA, *The numerical simulation of two-dimensional fluid flow with strong shocks*, J. Comput. Phys., 54 (1984), pp. 115–173.